Pseudo-random modulation continuous wave narrowband sodium temperature/wind lidar

Xin Fang[1,2,3#], Feng Li[1#], and Lei-lei Sun[1], Tao Li[1,2,3, *]

[1]Deep Space Exploration Laboratory/School of Earth and Space Sciences, University of Science and Technology of China, Hefei, Anhui, China

[2]CAS Key Laboratory of Geospace Environment, School of Earth and Space Sciences, University of Science and Technology of China, Hefei, Anhui, China

[3]CAS Center for Excellence in Comparative Planetology, University of Science and Technology of China, Hefei, Anhui, China

# These authors contributed equally to this work

*Correspondence to: litao@ustc.edu.cn

Abstract: We report the first Pseudo-random Modulation Continuous Wave (PMCW) narrowband sodium temperature/wind lidar developed at the University of Science and Technology of China (USTC). The laser system uses an 1178nm diode seed-laser and a fiber Raman amplifier with a fiber-coupled Acoustic Optical Modulator (AOM) to generate a narrowband 589.158 nm light with an output power of 1.5 W at 3 frequencies of v_0, v_+, and v_-. Based on an innovative technique and algorithm, the main beam and the residual beam modulated by Electro-Optic Modulator (EOM) with M-code are separately directed to the vertical and eastward directions. The 3-frequency light is designed in timing with the multiple-period 127-bit M-code groups. The uncertainties of the temperature and wind with the vertical and temporal resolutions of 1 km and 30 min/1hr under the clear-sky condition are estimated to be 5.0 K and 10 m/s, respectively at the sodium peak. The temperature and wind results are in good agreement with those observed by satellite and nearby ground-based meteor radar, demonstrating the reliability of the PMCW narrowband sodium lidar system for measuring the mesopause region temperature and wind.

1. Introduction

Temperature and wind are important atmospheric parameters for studying wave dynamics in the mesopause region, such as gravity waves, atmospheric tides, and planetary waves. Pulsed narrowband sodium lidar can measure the mesopause region temperature and wind with high temporal and vertical resolutions. With the development of laser technology, pulsed narrowband sodium lidar has been gradually developed and improved. Gibson and Thomas first measured sodium ground-state hyperfine structure and the mesopause temperature with an accuracy of 15K near the peak of the sodium layer (Gibson et al., 1979). Using a dye laser pumped by excimer, Fricke and von Zahn (1985) obtained 5K accuracy of temperature measurements with a vertical resolution of 1km and a temporal resolution of 10 minutes.

She et al. developed a high spectral resolution narrowband sodium lidar system using dual-frequency technology (She et al., 1992). Subsequently, 3-frequency technology was applied in their lidar for simultaneous temperature and wind measurements

in the MLT region (She et al., 2003). Hu et al. (2011) reported a mobile narrowband sodium lidar with temperature measurements. Li et al. (2012) constructed a narrowband sodium lidar with several technical improvements and obtained simultaneous temperature and wind results. Flashlamp pumped solid-state 589nm laser or solid-state 589nm seed laser based on Raman fiber amplifier was applied in pulsed narrowband sodium lidar (Xia et al., 2017; Yang et al., 2018). All-solid-state sodium lidar systems based on the sum frequency of pulsed 1064nm and pulsed 1319nm were developed to detect the mesopause region temperature and wind (Kawahara et al, 2002, 2017).

However, pulsed lasers, either dye or solid in the pulsed sodium lidars, cannot meet the space-borne platform due to size, weight, and power consumption limitations. Therefore, developing a lightweight and small-size narrowband sodium lidar is necessary for airborne and space-borne purposes. Referring to an idea of continuous wave (CW) in the application of microwave radar (Ridenour et al., 1948), CW lidar is a feasible miniaturized and lightweight lidar system. Takeuchi et al. (1986) first developed a CW aerosol lidar with ranging capability using M pseudo-random sequence code (M-code) modulated CW laser sources. Abo and Nagasawa (1984) proposed a random modulation CW lidar for Na layer detection. She et al. (2012) gave a detailed simulation of pseudorandom modulation continuous-wave (PMCW) sodium lidar for temperature and wind measurements in the mesopause region and pointed out that PMCW sodium lidar can achieve a signal-to-noise ratio comparable to pulsed sodium lidar. Li et al. (2021) implemented a PMCW single-frequency sodium lidar for sodium density measurement using an M-code modulated diode 589nm laser.

This study aims to develop a PMCW 3-frequency narrowband sodium lidar for simultaneous temperature and wind measurements in the mesopause region. The detection principle of PMCW narrowband sodium lidar (PMCW-NSL) is described in section 2. The system structure of PMCW-NSL is presented in section 3. Section 4 discusses the returning signals and temperature and wind results, followed by a summary in section 5.

2. The detection principle of PMCW-NSL

The PMCW-NSL mainly utilizes pseudorandom M-code a_i to modulate the CW laser beam and decodes returned signals by the cross-correlation between a_i and its inverse code $a_i^{'}$. The cross-correlation of the M-code has been described in the early simulation by She et al. (2012) and sodium density measurements by Li et al. (2021). It can be given out as below,

$$\phi_{aa'}(k) = \sum_{i=0}^{N-1} a_i a_{i+k}^{'} = \begin{cases} \dfrac{(N+1)}{2} & (k=0) \\ 0 & (k \neq 0) \end{cases} \tag{1}$$

According to the cross-correlation, we can obtain the decoded (inverted) signal with range resolution information as follows,

$$R_j = \frac{(N+1)}{2} \frac{P_0}{h\nu} G_j + B \tag{2}$$

where P_0 is the CW laser power; $h\nu$ is the energy of a single photon; G_j (Li et al., 2021) is the atmospheric response of the lidar system at altitude h_j ($h_j = j \cdot c \cdot \Delta t / 2$, c is the speed of light and Δt is the length of time for a single code α_i) and B is

the average intensity of background noise in Δt.

When the M code value is 1, the CW beam is transmitted from the polarization crystal inside the electro-optic modulator (EOM). When the M code value is 0, the CW laser is reflected by the polarization crystal. We refer to the transmitted light as the main light and the reflected output light as the residual light. Since the M-code has approximately the same number of occurrences of 0 and 1 in one cycle, this means that half of the energy of the CW laser is lost due to modulation. To improve the utilization efficiency of laser power, an innovative method is proposed for residual light detection under certain conditions and achieving the complete use of CW laser.

Since the principle of CW modulation by EOM is based on the assumption that there is no light loss under ideal conditions, the sum of the main and residual light should equal the intensity of the incident light (West et al., 1951). If the modulation sequence of the main light is the M-code sequence a_i, and the residual light sequence is b_i, then the relationship between b_i and a_i is given below:

$$b_i = 1 - a_i \tag{3}$$

Similar to the M-Code sequence, we also establish the inverted code of the residual light sequence as:

$$b_i' = 2b_i - 1 \tag{4}$$

By substituting Equation (3) into (4), we can obtain

$$b_i' = 2(1 - a_i) - 1 = -a_i' \tag{5}$$

where a_i' is the inverted code for a_i. The cross-correlation function between the residual light sequence and its inverted code can be calculated according to Equations (3) and (5):

$$\emptyset_{bb'}(k) = -1 + \sum_{i=0}^{N-1} a_{i+k}\, a_{i'} \tag{6}$$

By substituting the cross-correlation function (Equation (1)) of the M sequence into the above equation, the cross-correlation function of the residual light code sequence can be obtained:

$$\phi_{bb'}(k) = \begin{cases} \dfrac{(N-1)}{2} & (k = 0) \\ -1 & (k \neq 0) \end{cases} \tag{7}$$

Table 1 Sequences of residual light code, its associated receiving code, and their correlation for N = 31

i	0	1	2	3	4	5	6	7	8	9	10	11	12	13	14	15
b_i	0	0	0	0	0	0	0	1	0	1	0	1	0	1	1	0
b_i'	-1	-1	-1	-1	-1	-1	-1	1	-1	1	-1	1	-1	1	1	-1
$\phi_{bb'}(i)$	63	-1	-1	-1	-1	-1	-1	-1	-1	-1	-1	-1	-1	-1	-1	-1
i	16	17	18	19	20	21	22	23	24	25	26	27	28	29	30	31
b_i	0	1	1	0	0	0	1	0	0	0	1	0	1	1	0	1
b_i'	-1	1	1	-1	-1	-1	1	-1	-1	-1	1	-1	1	1	-1	1
$\phi_{bb'}(i)$	-1	-1	-1	-1	-1	-1	-1	-1	-1	-1	-1	-1	-1	-1	-1	-1

Table 1 shows the values of the residual light code, inverted code, and cross-correlation function. The inverted codes satisfy

the autocorrelation property of pseudo-random coding. Although the correlation function results differ from the M-code, they can also be used for CW laser detection under certain conditions.

Similar to the M sequence, residual light is modulated by the residual light sequence b_i to CW, and then the acquisition signal equation can be obtained:

$$S_i = \frac{P_0}{h\nu} \sum_{k=0}^{N-1} (G_k b_{i-k}) + B \tag{8}$$

For a single acquisition cycle time, the sky background noise signal is nearly constant, and the system noise signal is replaced with a constant signal. Similar to the main light, the acquired signal above is decoded by the one-to-one inverse code of the residual light sequence, and the new inverted signal R_m at altitude h_m ($h_m = m \cdot c \cdot \Delta t/2$, where c is the speed of light and Δt is the length of time for a single code $b_{i'}$) can be obtained as follows:

$$R_m = \frac{P_0}{h\nu} \sum_{i=0}^{N-1} (b'_{i-m} S_i) = \frac{P_0}{h\nu} \frac{(N+1)}{2} G_m - \frac{P_0}{h\nu} \sum_{k=0}^{N-1} G_k - B \tag{9}$$

Comparing the decoded signals from the M code, we can find several differences in the final form of Equation (9) from Equation (1): there is an additional term in the decoded signal. This term is always a negative constant when computing the decoded signal of any given height. The background signal is also negative. The decoded signals are just the altitude-returned signals superimposed with a large negative background. Consequently, when CW lidar detection is performed using residual light, the background noise cannot be directly acquired in the decoded signal. To solve this issue, we add an additional zero-set code period to the M code to explicitly measure the background noise signal.

3. PMCW-NSL system

The PMCW-NSL system consists of a transmitter with a CW laser modulated by an M-code, a receiver with two Newtonian telescopes, and a specifically designed acquisition and timing subsystem. The schematic diagram of the PMCW-NSL system is shown in Figure 1.

The transmitter is to generate an M-code modulated 589nm CW laser and send it into the atmosphere. In cooperation with Shanghai Frequency Calibration Co., LTD., we have developed an all-solid-state CW laser source suitable for PMCW-NSL based on fiber Raman laser technology (Murray et al., 1998; Feng et al., 2004; Taylor et al., 2010)). Its basic principle is shown in Figure 1, and its physical photo is shown in Figure 2. A narrowband diode 1178nm continuous laser with a linewidth of ~50kHz and power of 30 mW (TOPTICA DL Pro, tunable diode laser) acts as the seeder injected into the fiber Raman amplifier with two-stage fiber Raman amplification. The first stage of the fiber Raman amplifier amplifies the 1178 nm seed laser to about 150 mW, divided into two outputs, one for laser frequency locking and the other for the input of the secondary amplification after frequency shift by fiber Acoustic-Optic Frequency Shifter (AOFS). The laser frequency locking is

completed by a Doppler-free saturated absorption system with an accuracy of ± 1MHz. The fiber AOFS consisted of two AOMs and two optical switches shift laser frequency 0 MHz, +315 MHz, and -315 MHz respectively at 1178.316 nm (corresponding frequency shifts 0 MHz(v_0), +630 MHz(v_+) and -630 MHz(v_-) at 589.158nm after passing the Second-Harmonic-Generator (SHG) which is Periodically polarized lithium niobate (PPLN)) crystal. The power of an amplified 589 nm laser is ~1.5 W at v_0, v_+ and v_- frequencies. Notably, the optical fiber Raman amplifier only weighs ~25kg and consumes power ~450 Watts, clearly superior to the laser used in pulsed sodium lidar.
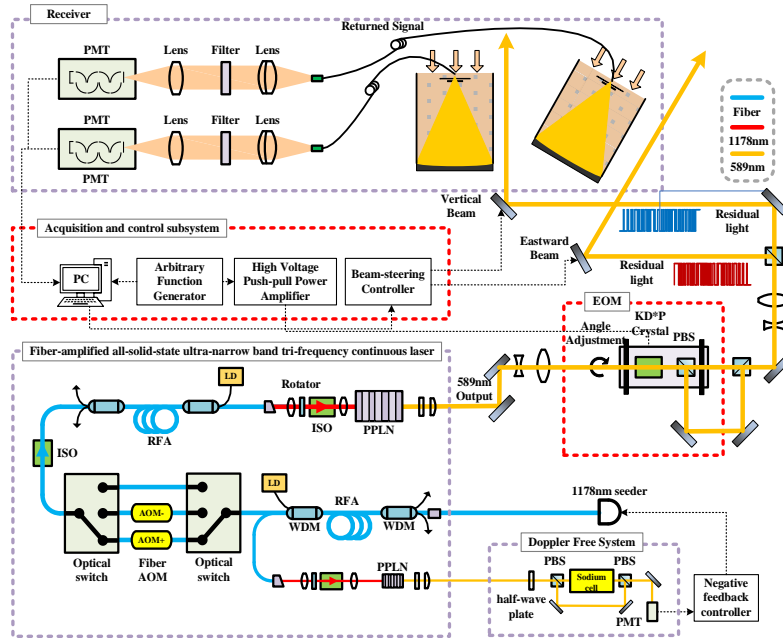
Figure 1 Schematic diagram of PMCW -NSL system
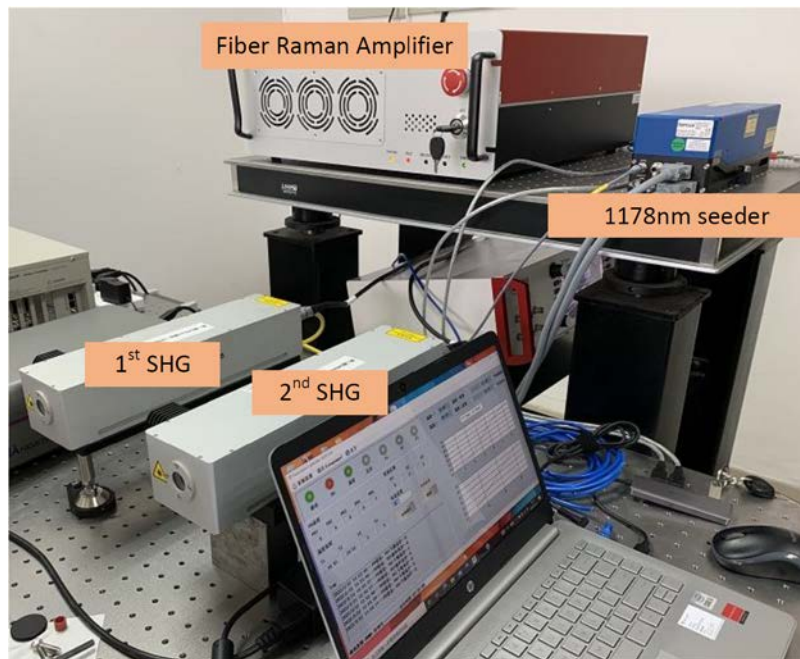
Figure2 Photo of the fiber Raman amplifier

M-code then modulates the amplified 589nm laser via an electro-optic modulator (EOM). Both the main light and the residual light are directed to the atmosphere in the vertical and eastward directions respectively. To eliminate the effects of the inverted signals of the strong Rayleigh returned signal scattered from the lower atmosphere called "ghost targets," we send the laser beam at a distance of 9m from the receiving telescope and align the sending/receiving optics axis using automatic collimation system with an accuracy of ~10 $urad$ [6]. The key parameters of the PMCW-NSL system are given in Table 2.

125

Table 2 Technical specifications of the PMCW -NSL

Transmitter		
Seeder	Center wavelength	1178.316nm
	Coarse tuning range	1178nm±4nm
	Mode hop-free tuning range	10GHz
	Power	50mW
	linewidth	50kHz
	Output interface	Fiber coupler
Fiber Raman amplifier include fiber AOFS	Center wavelength (nm)	1178.316nm
	Operation mode	Continuous wave
	AOFS mode	Fixed frequency
	AOFS value	0, +315MHz, -315MHz @1178nm (Corresponding to 0, +630MHz, - 630MHz@589nm)
	AOFSr switching rising and falling time	<1us
	First 1178 nm laser power (W)	7.4
	First 589 nm laser power (W)	1.5, 1.5,1.5 @0, +630MHz, -630MHz
	Second 589 nm laser power (mW)	50
	Power adjustment range (%)	10-100
	Power stability of the first 589 nm laser (%)	RMS: 0.68
	Cooling	Air
	Electrical power	220V, 2A
	Weight	25 kg
EOM	Crystal type	KD*P Crystal
	Aperture	<2.7mm
	Coating	400-800 nm
	Transmission	>85%
	Extinction ratio	300:1-500:1

	Bandwidth	DC-to-30MHz
	Rise Time (10%-90%)	8ns
Receiver and acquisition subsystem		
Telescope	Type	Newtonian primary focus
	Diameter	30"
	F/#	F/2 for vertical and F/2.4 for Eastward
Fiber	Length	15m
	Core diameter	1.5mm
	Numerical Aperture	0.37
Interference filter	Central wavelength	589.1nm
	Bandpass	0.2nm
	Transmission	~70%
Detector	Model	H7421
	Peak sensitivity wavelength	580nm
	Quantum efficiency	~40%@580nm
Photon counter	Model	P7882
	Typical counting rate	350MHz

130

The receiver of PMCW-NSL includes two Newtonian prime-focus telescopes, pointing in the zenith direction and eastward at 20° tilted from the zenith. The returned signal from each telescope is acquired after 10m length optic fiber transmission, lens collimation, filtering by an optical filter, lens convergence, and photoelectric conversion process. The main parameters of the receiver are shown in Table 1.

135 The timing control for the PMCW-NSL is one of the major technical challenges ensuring lidar obtains returned signals effectively. It is mainly composed of two parts. One is responsible for coding the CW laser and trigging the acquisition; the other is for switching the laser beam, and tagging returned signals in 3 frequencies. The timing diagram of PMCW -NSL is shown in Figure 3. A TTL signal(S1) with a frequency of 3Hz generated by the signal generator acts as the main synchronization clock of the system. S1 triggers one self-developed FPGA circuit board at a frequency division of 3 to generate

140 3 TTL signals (S2, S3, and S4) with a pulse width of S1 period length as the control signals of 3-frequency switching of fiber AOM and the spectrum tagging signals of photon counter. S1 also externally triggers a DG645 to generate 23 TTL pulsed signals as the external trigger of the photon counter and an arbitrary waveform generator (AWG). The AWG produces one M-code group with 14 periods 127 M-code and 2 periods zero-set 127 M-code and a short idle time in one cycle. A 7 μs time length for a single code corresponds to a range resolution of 1.05 km.

145 The total detection range of the 127 M code is, therefore, 127×1.05≈133 km. The time length of 23 M-code groups is just slightly less than the S1 period. PMCW-NSL alternatively sends a laser in M-code groups of 3-frequency in 3 Hz and receives the respective returned signal. The detailed design of the M-code group was illustrated in our previous work [05]. It is noted

that the S5 and S6 signals in one S1 cycle are zoomed in in Figure 3.
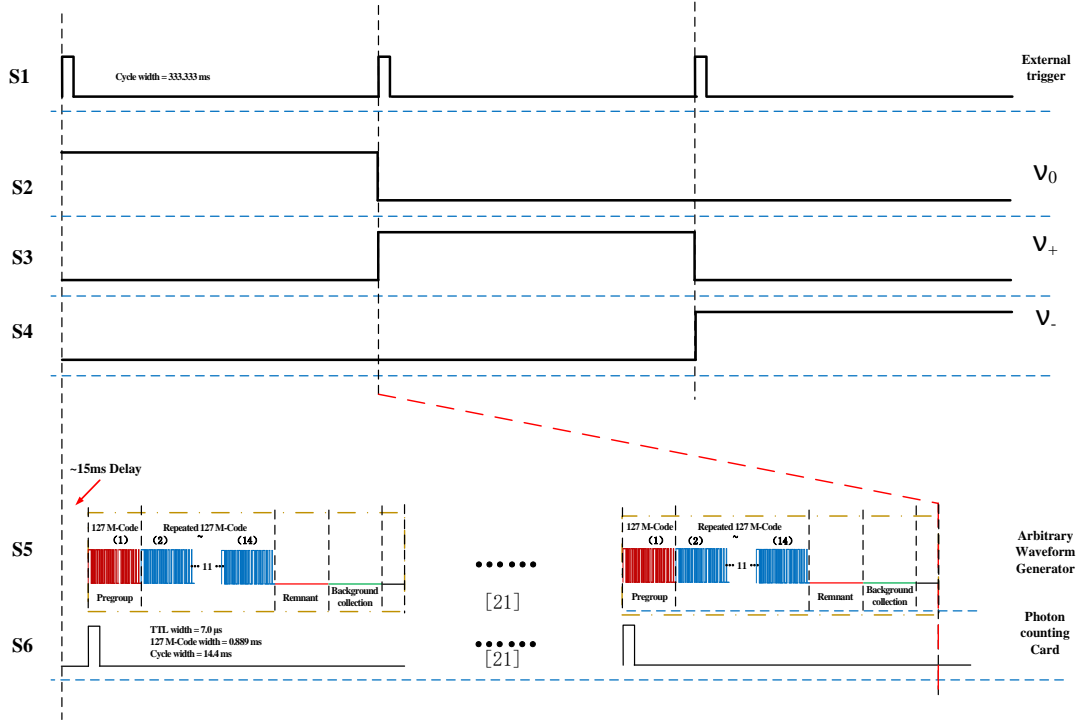
Figure 3 Timing diagram of PMCW -NSL

4. Signals and results

PMCW-NSL acquires backscattering return signals of 3 frequencies (v_0, v_+ and v_-) in five minutes with 2048 bins and 7us bin width. We first sum up signals of 127 M-code cycles at the same code bin in five minutes and then decode these signals to obtain range-resolved profiles. An example of the 3-frequency signals observed by PMCW -NSL that accumulated from 10:22UT to 10:26UT on November 24, 2021, is shown in Figure 4. Figure 4(a) shows the raw 3-frequency signals with a spatial resolution of 1.05km and a temporal resolution of 5 min. According to equation (7), the inverted signal profile with range resolution information and background removal similar to that obtained by pulsed sodium lidar is shown in Figure 4(b). It is noted that the removal background includes background shift and pure background shot noise acquired at the second period of zero-set 127 M codes. Figure 4(c) and Figure 4(d) are the signal profiles in the sodium layer and corresponding signal-to-noise ratios (SNRs). The number of returned signal photons in 3 frequencies reach 1×10^5, 5×10^4, and 5×10^4, respectively, at the peak altitude of the sodium layer with SNRs larger than 30, 15, and 15 respectively.
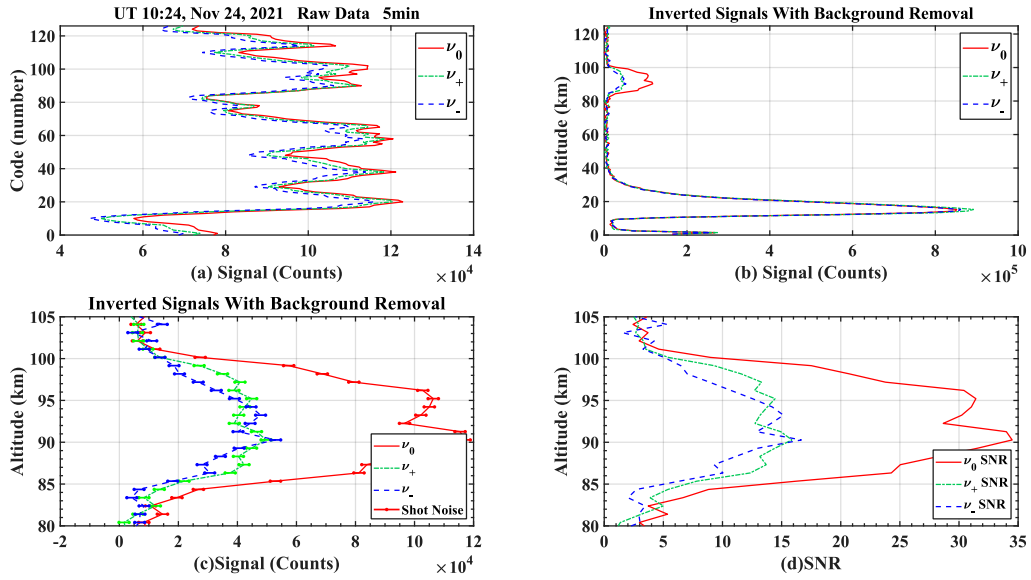
Figure 4 Profiles of (a) raw signals arranged in m-code sequence with 1.05 km spatial and 5 min temporal resolutions on November 24, 2021, (b) inverted signals with background subtracted, (c) inverted signals of only the sodium layer region, and (d) the signal-to-noise ratio of at v_0, v_+, v_- frequencies of PMCW -NSL.
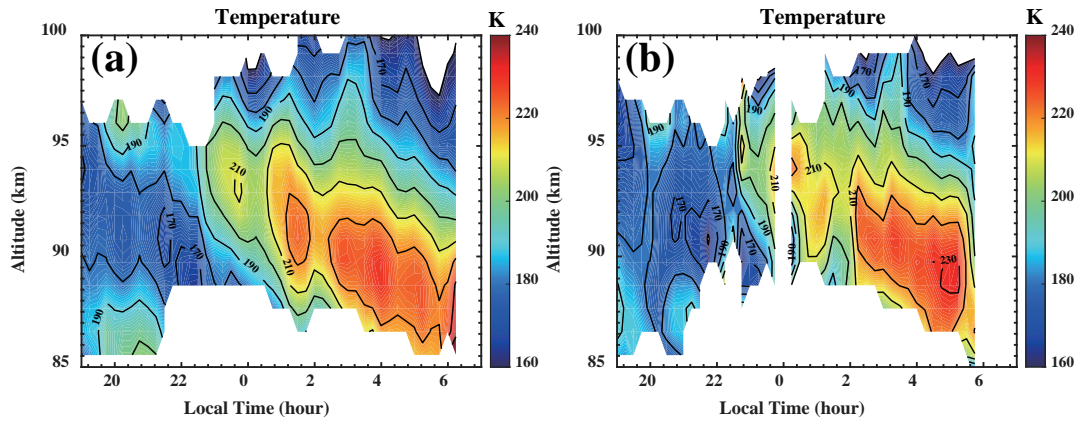
Figure 5 Temperature contour observed by PMCW-NSL on November 24, 2021, in (a)vertical and (b)eastward directions.

Since the SNR of PMCW-NSL is lower than that of pulse lidar at the same power, photon counts are accumulated for at least 15 minutes to improve the SNR. Figure 5 shows the nighttime temperature contour results with a time resolution of 15 min. The temperature varied from 160 to 240K during the night, and an apparent wave structure with a downward phase can be seen, suggesting possible modulation by tides. The white part in the contour indicates that the temperature uncertainty is greater than 25 K or the signal SNR is insufficient, and the temperature results within are invalid. The temperature uncertainty is about 5 K near the peak of the sodium layer (90-95 km), while larger than 25 K at the edge of the sodium layer.
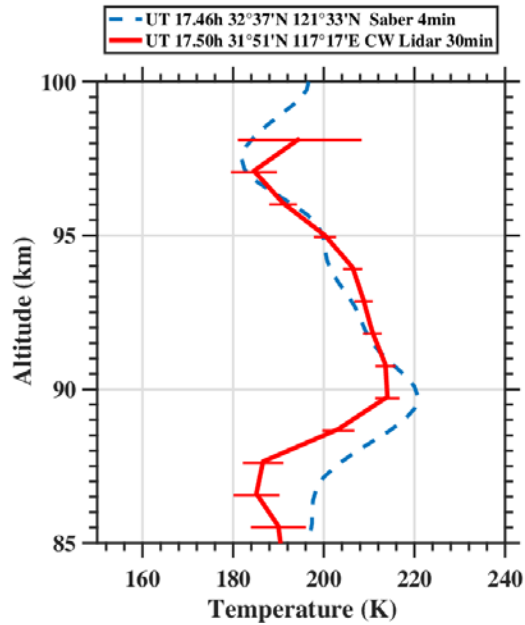
Figure 6 Comparison of temperature profiles between PMCW -NSL (red solid line) and SABER (blue dashed line).

180

Because our pulsed narrowband sodium temperature/wind lidar cannot simultaneously run with PMCW-NSL, we compare the PMCW-NSL temperature results at 12:30 UT (20:30 LT) with the SABER observation on November 30, 2021, as shown in Figure6. The temporal and vertical resolutions of PMCW-NSL results are 30 minutes and 1km, respectively, while those for SABER results are 2 minutes and 2 km. The temperature observed by the PMCW-NSL is in generally good agreement with

185 the SABER. But there are slight differences in absolute values, significantly below 90km and above 97km. One possible reason for these differences could be the difference in measurement locations and resolutions.
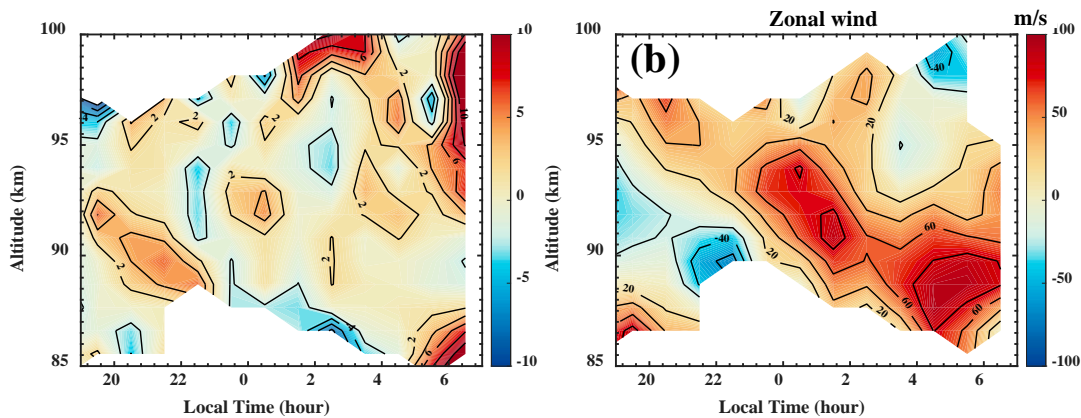
Figure 7 (a)Vertical wind and (b)zonal wind observed by the PMCW-NSL on November 24, 2021.

190

The vertical and zonal winds observed by PMCW-NSL on November 24, 2021, are shown in Figure 7. The vertical resolution of the data is 1 km, and the temporal resolution is 1 hour. The white region in the contour indicates that the wind error at this

point is greater than 20m/s, which is considered an unreliable result. Figure 7 (b) shows that the zonal winds at 87-97 km are about -20~100 m/s, and the error is large at the edge of the sodium layer due to low SNR. From the zonal wind, the contour shows an obvious downward phase progression, likely related to the solar tides. From the vertical wind profiles shown in Figure 8, the vertical wind fluctuates within ±5 m/s overnight, and the nightly mean of the vertical wind velocity is close to 0. This is in good agreement with other vertical wind observations (White et al., 1999). The error bars of the nightly mean vertical wind velocity in Figure 8 represent the measurement uncertainties due to statistical noise.
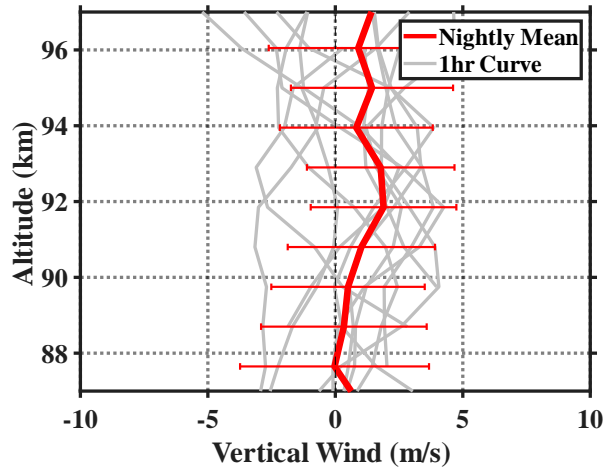
Figure 8 Vertical wind profiles of PMCW-NSL on November 24, 2021.
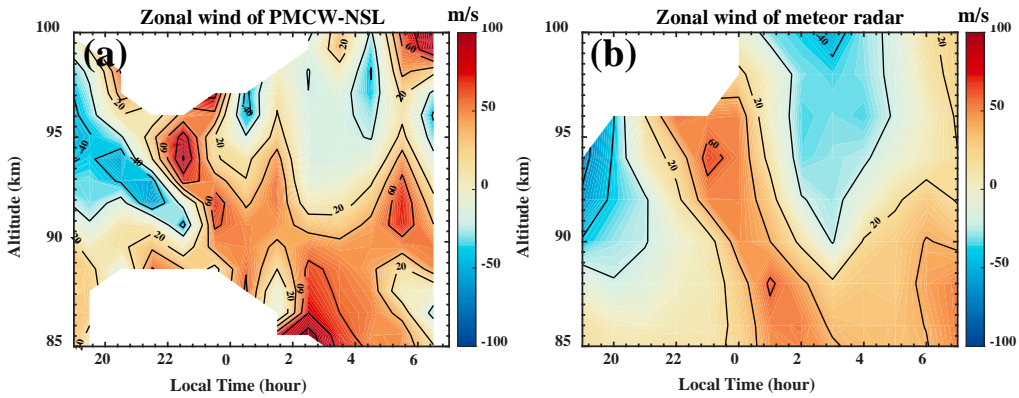
Figure 9 Zonal wind contour of (a) PMCW-NSL with a vertical resolution of 1km and temporal resolution of 1hr and (b) meteor radar with a vertical resolution of 2km and a temporal resolution of 1hr on December 1, 2021.
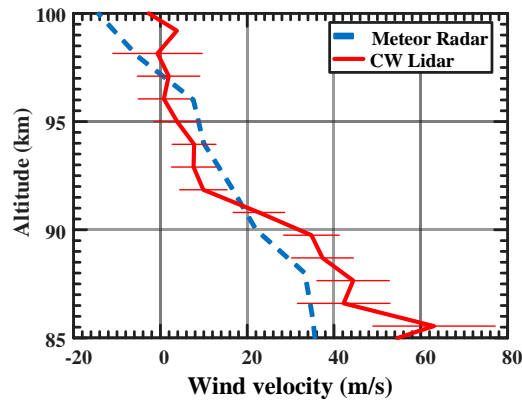
Figure 10 Comparison of nightly mean zonal wind profile between of PMCW-NSL (red solid line) and Meteor radar (blue dash line) on December 1, 2021.

Figure 9 compares zonal winds on December 1, 2021, observed by PMCW-NSL, with those observed by a meteor radar located at ~200km northwest of the lidar site. The uncertainty of zonal wind observed by the PMCW-NSL is less than 10 m/s at the sodium peak and ~25m /s at the edge of the sodium layer. The uncertainty of zonal wind observed by the meteor radar for 1 hour average is less than 5m/s at 86km (Zeng et.al., 2022). Both observations suggest similar variations in time and structure. The downward phase progression of the semidiurnal tide is clear in both plots. The zonal wind maximum of 100 m/s observed by PMCW-NSL appears earlier than that of 80m/s by meteor radar. Figure 10 compares the nightly mean zonal wind profile of the PMCW-NSL (solid red line) and meteor radar (dashed blue line) on December 1, 2021. The zonal wind of the PMCW-NSL shows a good agreement with that of the meteor radar.

5. Summary

We successfully developed the first PMCW-NSL system for simultaneous measurements of the mesopause region temperature and wind. The lidar system adopted a diode 1178nm seeder and a co-developed fiber Raman amplifier with a fiber-coupled AOM inside to obtain a 589nm light at 3 frequencies with almost the same power, which outputs on the same path. An EOM was introduced to modulate the 589nm laser in M-code. Based on the innovative decoded technique and algorithm for CW lidar, both the main and the residual lights modulated by M-code are used and directed to the atmosphere in the vertical and eastward direction tilted 20ºfrom the zenith. Two Newtonian telescopes with a diameter of 30 inches in corresponding pointing are used to receive the returned signals. The 3-frequency laser is emitted out sequentially triggered at 3Hz in external mode. In one period of the external trig, the special M-code group consisted of 14 periods 127 M-code and 2 periods zero-set 127 M-code, and a short idle time is designed to acquire valid returned signals and pure background noises.

Using the PMCW-NSL system, we successfully retrieved the mesopause region temperature and wind with uncertainties of ~5K and ~10m/s at the peak of the sodium layer. The temperature comparison between PMCW-NSL observation and SABER observation shows good agreement with slight differences. The zonal wind results observed by PMCW-NSL also agree with

those observed by a nearby meteor radar. These demonstrate that the PMCW-NSL can reliably measure the mesopause region temperature and wind. In the future, we plan to improve its accuracy and resolution by implementing a 20W 589nm CW laser in the PMCW-NSL system.

Data availability. The PMCW-NSL data at Hefei are available by contacting the corresponding author. We will upload the data to the National Space Science Data Center, National Science & Technology Infrastructure of China. The wind data of the meteor radar can be applied from the National Space Science Data Center, National Science & Technology Infrastructure of China (http://www.nssdc.ac.cn/eng). The SABER temperature data are available at http://saber.gats‑inc.com/.

Author contributions. XF wrote the paper and provided technical guidance for lidar development. FL developed the lidar system and retrieved the data. LS retrieved the data. TL designed the experiment, contributed to the discussion and revision of the paper, and explained the results.

Competing interests. The author has declared that there are no competing interests.

Disclaimer. Publisher's note: Copernicus Publications remains neutral with regard to jurisdictional claims in published maps and institutional affiliations.

Acknowledgments. We acknowledge Wen YI provides wind data of the meteor radar, which can be applied from the National Space Science Data Center, National Science & Technology Infrastructure of China (http://www.nssdc.ac.cn/eng). We thank the SABER team for making the SABER temperature dataset available at http://saber.gats‑inc.com/. The authors would like to thank Chiao-Yao She for the helpful discussion.

Financial support. National Natural Science Foundation of China (42130203, 41974177, 41974175). The B-type Strategic Priority Program of the Chinese Academy of Sciences Grant No. XDB41000000. The pre-research project on Civil Aerospace Technologies No. D020105 funded by China's National Space Administration.

References:

Abo, M. and Nagasawa, C.: Random modulation CW dye lidar for measuring mesospheric sodium layer, the 17th International Laser Radar Conference, Sendai, Japan, 25–29, p258, 1984.

Feng, Y., Huang, S., Shirakawa, A., and Ueda, K.: 589 nm light source based on Raman fiber laser, Japanese Journal of Applied Physics Part 2-Letters & Express Letters, 43, L722-L724, https://doi.org/10.1143/JJAP.43.L722, 2004.

Feng, Y., Taylor, L., and Calia, D. B.: Multiwatts narrow linewidth fiber Raman amplifiers, Opt. Express, 16, 10927-10932, https://doi.org/10.1364/OE.16.010927, 2008.

Fricke, K. H., and vonZahn, U.: Mesopause temperature derived from probing the hyperfine structure of the D2 resonance line of sodium by lidar, J. Atmos. Terr. Phys. 47, 499-512 , https://doi.org/10.1016/0021-9169(85)90116-3, 1985.

Gibson, A., Thomas, L., and Bhattachacharyya, S.: Laser observation of ground-state hyperfine structure of sodium and of temperatures in the upper atmosphere, Nature (London) 281, 131-132, https://doi.org/10.1038/281131a0, 1979.

Hu, X., Yan, Z. A., Guo, S. Y., and Cheng Y.: Sodium fluorescence Doppler lidar to measure atmospheric temperature in the mesopause region, Chinese Sci. Bull, 56, https://doi.org/10.1007/s11434-010-4306-x, 2011.

Kawahara, T. D., Kitahara, T., Kobayashi, F., Saito, Y., Nomura, A., She, C.-Y., Krueger, D. A., and Tsutsumi, M.: Wintertime mesopause temperatures observed by lidar measurements over Syowa station (69°S, 39°E), Antarctica, Geophys. Res. Lett. 29(15), 1709, https://doi.org/10.1029/2002GL015244, 2002.

Kawahara, T. D., Nozawa, S., Saito, N., Kawabata, T., Tsuda, T. T., and Wada, S.: Sodium temperature/wind lidar based on laser-diode-pumped Nd:YAG lasers deployed at Tromso, Norway (69.6 degrees N, 19.2 degrees E), Opt. Express 25(12), A491-A501 , https://doi.org/10.1364/OE.25.00A491, 2017.

Li, T., Fang, X., Liu, W., Gu, S. Y., and Dou, X.: Narrowband sodium lidar for the measurements of mesopause region temperature and wind, Appl. Opt. 51(22), 5401–5411, https://doi.org/10.1364/AO.51.005401, 2012.

Li, F., Li, T., Fang, X., Tian, B., and Dou, X.: Pseudo-random modulation continuous-wave lidar for the measurements of mesopause region sodium density, Optics Express 29(2), 1932-1944, https://doi.org/10.1364/OE.410852, 2021.

Murray, J. T., Roberts, W. T., Austin, W. L., Powell, R. C., and Bonaccini, D. : Fiber Raman Laser for sodium guide star, Adaptive Optical System Technologies, Parts 1 and 2, 3353, 330-339, https://doi.org/10.1117/12.321725, 1998.

Ridenour, L., Glasoe, G. N., Lebacqz, J. V., Collins, G. B., Greenwood, I. A., Holdam, J. V., Macrae, D., and Pierce, J. R.: MIT Radiation Laboratory Series, Phys. Today, 1948.

She, C. Y., Yu, J. R., Latifi, H., and Bills, R. E.: High-Spectral-Resolution Fluorescence Lidar for Mesospheric Sodium Temperature Measurements, Appl. Opt., 31, 2095-2106 , https://doi.org/10.1364/AO.31.002095, 1992.

She, C. Y., Sherman, J., Yuan, T., Williams, B. P., Arnold, K., Kawahara, T. D., Li, T., Xu, L., J. Vance, D., and Krueger, D. A.: The first 80-hour continuous lidar campaign for simultaneous observation of mesopause region temperature and wind, Geophys. Res. Lett., 30(6), 1319, https://doi.org/10.1029/2002GL016412, 2003.

She, C. Y., Abo, M., Yue, J., Williams, B. P., Nagasawa, C., and Nakamura, T.: Mesopause-region temperature and wind measurements with pseudorandom modulation continuous-wave (PMCW) lidar at 589 nm, Appl. Opt. 51(12), 1981, https://doi.org/10.1364/AO.50.002916, 2012.

Takeuchi, N., Baba, H., Sakurai, K., and Ueno, T.: Diode-laser random-modulation cw lidar, Appl. Opt. 25(1), 63–67, https://doi.org/10.1364/AO.25.000063, 1986.

Taylor, L. R., Feng, Y., Calia, D. B.: 50W CW visible laser source at 589nm obtained via frequency doubling of three coherently combined narrow-band Raman fibre amplifiers, Opt. Express, 18, 8540-8555, https://doi.org/10.1364/OE.18.008540, 2010.

West C. D. and Jones, R. C.: On the Properties of Polarization Elements as Used in Optical Instruments .1. Fundamental Considerations, Journal of the Optical Society of America, 41, 976-982, https://doi.org/10.1364/JOSA.41.000976, 1951.

White M. A.: A frequency-agile sodium lidar for the measurement of temperature and velocity in the mesopause region, Ph. D. Thesis, Colorado State University, America, 129 PP, 1999.

Xia, Y., Du, L. F., Cheng, X. W., Li, F. Q., Wang, J. H., Wang, Z. L., Yang, Y., Lin, X., Xun, Y., Gong, S., and Yang, G.: Development of a Solid-State Sodium Doppler Lidar Using an All-Fiber-Coupled Injection Seeding Unit for Simultaneous Temperature and Wind Measurements in the Mesopause Region, Opt. Express 25(5), 5264-78, https://doi.org/10.1364/OE.25.005264, 2017.

Yang, Y. L., Yang, Y., Xia, Y., Lin, X., Zhang, L., Jiang, H. W., Cheng, X. W., Liu, L., Ji, K., and L, F. Q.: Solid-State 589 Nm Seed Laser Based on Raman Fiber Amplifier for Sodium Wind/Temperature Lidar in Tibet, China, Opt. Express 26 (13), 16226-16235, https://doi.org/10.1364/OE.26.016226, 2018.

Zeng, J., Yi, W., Xue, X., Reid, I., Hao, X., Li, N., Chen, J., Chen, T. D., Dou, X. K.: Comparison between the MesosphericWinds Observed by Two Collocated Meteor Radars at Low Latitudes. Remote Sens. 14, 2354. https://doi.org/10.3390/rs14102354, 2022.